Modeling Extreme Mass Ratio Inspirals within the Effective-One-Body Approach

Nicolás Yunes,[1] Alessandra Buonanno,[2] Scott A. Hughes,[3] M. Coleman Miller,[4] and Yi Pan[2]

[1]*Department of Physics, Princeton University, Princeton, New Jersey 08544, USA*
[2]*Department of Physics, University of Maryland, College Park, Maryland 20742, USA*
[3]*Department of Physics and MIT Kavli Institute, Cambridge, Massachusetts 02139, USA*
[4]*Department of Astronomy, University of Maryland, College Park, Maryland 20742, USA*
(Received 23 September 2009; published 5 March 2010)

We present the first models of extreme-mass-ratio inspirals within the effective-one-body (EOB) formalism, focusing on quasicircular orbits into nonrotating black holes. We show that the phase difference and (Newtonian-normalized) amplitude difference between analytical EOB and numerical Teukolsky-based gravitational waveforms can be reduced to $\lesssim 10^{-1}$ rad and $\lesssim 2 \times 10^{-3}$, respectively, after a 2-year evolution. The inclusion of post-Newtonian self-force terms in the EOB approach leads to a phase disagreement of $\sim$6–27 rad after a 2-year evolution. Such inclusion could also allow for the EOB modeling of waveforms from intermediate-mass-ratio, quasicircular inspirals.

Introduction.—Extreme-mass-ratio inspirals (EMRIs) are the gravitational wave (GW) driven coalescences of stellar mass compact objects with supermassive black holes (SMBHs). When the large black hole's (BH's) mass is in the range $10^5 M_\odot$–$10^7 M_\odot$, EMRI waves are emitted at frequencies well suited to measurement by the planned Laser Interferometer Space Antenna (LISA). Because EMRI events are expected to be abundant [1] and will carry detailed information about strong-field spacetimes near SMBHs [2], they are high-priority targets for LISA observation. The intrinsic feebleness of these waves will require accurate waveform templates to detect and faithfully measure the signals produced by nature. Because EMRIs can spend thousands of cycles near the SMBH's innermost stable circular orbit (ISCO), the binary's orbital speed is $v/c \sim 0.1$–0.5, a regime where traditional post-Newtonian techniques perform poorly. Numerical models built using BH perturbation theory should be able to reliably model EMRI signals. However, the computational cost of covering the full span of EMRI parameter space (including effects of BH spin, nonequatorial orbits, and eccentricity) is likely to be very high [1].

This has motivated us to examine techniques for reliably approximating these waves at a much smaller computational cost. The effective-one-body (EOB) formalism was introduced as a way to analytically describe the inspiral, merger, and ringdown waves emitted by comparable-mass BH binaries [3,4]. This formalism was then extended to higher post-Newtonian (PN) orders [5], spinning BHs [6–8], small mass-ratio mergers [9,10], and was further improved by introducing factorized waveforms [10,11]. By calibrating a few adjustable parameters, [12,13] showed that the phase and amplitude of the EOB and numerical-relativity waveforms can be made to agree within the numerical error of the simulations, thus providing GW detectors with faithful templates. In this analysis, we calibrate EOB with BH perturbation theory templates in order

to similarly model EMRI waves. Such an analysis must be done separately from the previous EOB-numerical relativity calibration, because numerical relativity simulations cannot yet model the tens or hundreds of thousands of orbits needed to describe EMRI signals.

As a first step, we restrict our models to a small compact object spiraling along a quasicircular orbit into a nonspinning SMBH [14]. Although the assumptions of circularity and zero spin can and will be relaxed in the future, there exist astrophysical motivations for this initial choice of binary configuration. For example, the tidal separation scenario for EMRIs [15] implies nearly circular but arbitrarily inclined orbits in the $>10^{-4}$ Hz frequency band relevant for LISA, and the accretion disk capture picture [16–18] implies orbits that are both nearly circular and in the equatorial plane of the SMBH. In addition, the characteristics of the SMBHs themselves are uncertain in the $<10^7 M_\odot$ mass range most relevant for LISA. In some astrophysical scenarios, the growth of these BHs is dominated by the accretion of stars moving on random trajectories, instead of by the accretion of gas disks, thought to be more important for higher-mass SMBHs [19]. Such growth would lead to $\hat{a} \equiv |\vec{J}|/M^2 \ll 1$ (in natural units with $G = c = 1$, which we use throughout this Letter). The nonrotating spacetime is a reasonable first approximation.

We now systematically compare EMRI waveforms computed in the EOB approach to those calculated using BH perturbation theory via numerical solution of the Teukolsky equation [20–22]. As we describe in the remainder of this Letter, we find that appropriately calibrated EOB waveforms do an excellent job modeling waves computed using BH perturbation theory. This suggests that the EOB scheme can be an outstanding tool for modeling EMRI waves in future LISA data analysis.

Analytical and numerical modeling.—For a BH binary with masses m_1 and m_2, we set $M = m_1 + m_2$ and $\mu = m_1 m_2/M = \nu M$. In the absence of spins, the motion is

constrained to a plane. Let us introduce Schwarzschild-like coordinates (r, Φ) (where r is M normalized) centered on the binary's center of mass, as well as their reduced (μ normalized) conjugate momenta (p_r, p_Φ). The non-spinning EOB Hamiltonian then reads [3] $H^{\text{real}} = M\sqrt{1 + 2\nu[(H^{\text{eff}} - \mu)/\mu]} - M$, where the effective Hamiltonian is [3,5,10]

$$H^{\text{eff}} = \mu\sqrt{p_{r_*}^2 + A(r)\left[1 + \frac{p_\Phi^2}{r^2} + 2(4 - 3\nu)\nu\frac{p_{r_*}^4}{r^2}\right]}. \quad (1)$$

We use here the reduced conjugate momentum p_{r_*} to the EOB tortoise radial coordinate r_* because it improves the numerical stability of the code [10]. The tortoise coordinate is defined via $dr_*/dr = \sqrt{D(r)}/A(r)$, where $A(r)$ and $D(r)$ are obtained by applying the Padé resummation [5] to the Taylor-expanded forms [3,5] $A_T(r) = 1 - 2/r + 2\nu/r^3 + (94/3 - 41\pi^2/32)\nu/r^4$, $D_T(r) = 1 - 6\nu/r^2 + 2\nu(3\nu - 26)/r^3$. The EOB Hamilton equations are written using reduced quantities $\hat{H}^{\text{real}} \equiv H^{\text{real}}/\mu$, $\hat{t} \equiv t/M$ [4]:

$$\frac{dr}{d\hat{t}} = \frac{A(r)}{\sqrt{D(r)}}\frac{\partial\hat{H}^{\text{real}}}{\partial p_{r_*}}, \qquad \frac{d\Phi}{d\hat{t}} = \frac{\partial\hat{H}^{\text{real}}}{\partial p_\Phi}, \quad (2)$$

$$\frac{dp_{r_*}}{d\hat{t}} = -\frac{A(r)}{\sqrt{D(r)}}\frac{\partial\hat{H}^{\text{real}}}{\partial r}, \qquad \frac{dp_\Phi}{d\hat{t}} = \hat{\mathcal{F}}_\Phi, \quad (3)$$

where $\hat{\mathcal{F}}_\Phi$ is a Padé-resummed radiation-reaction force [4,23], related to the GW energy dissipation to be defined later. Initial data are found through a mock evolution, initialized at an orbital separation of $100M$ using initial conditions for a quasicircular inspiral [4].

With the EOB inspiral dynamics in hand, we compute the multipole-decomposed GW $h_{\ell m}$ (ℓ and m refer to spherical harmonics), following the factorized PN prescription of [11], which depends directly on orbital quantities. The EOB GW phase is computed by solving $\dot{\Phi}_{\ell m} = -(1/m)\text{Im}[\dot{h}_{\ell m}/h_{\ell m}]$. Errors in the EOB waveforms arise due to inaccuracies in the numerical solution of Eqs. (2) and (3) and inaccurate initial data. We have investigated such sources of error and estimate them to be no worse than $\delta\Phi_{22} \lesssim 0.03$ rad in the waveform's phase and $\delta h_{22}/h_{22} \lesssim 10^{-7}$ in the normalized amplitude after a 2-year evolution. This cumulative error is primarily dominated by the accuracy of the routine used in MATHEMATICA to solve Eqs. (2) and (3).

We compare EOB waves with waveforms computed in BH perturbation theory by solving the Teukolsky equation. We use the code described in [21] (modified with the spectral techniques of [24]) to construct the Newman-Penrose curvature scalar ψ_4. Our code computes $\psi_4 = R^{-1}\sum_{\ell m}Z_{\ell m-2}Y^{\ell m}(\theta, \phi)e^{-im\Omega t}$ where $-2Y^{\ell m}(\theta, \phi)$ is a spin-weight -2 spherical harmonic, Ω is the frequency of circular Schwarzschild orbits, and R is the distance from the center of mass to the observer. The amplitude $Z_{\ell m}$ is found by first building a Green's function to the radial Teukolsky equation, and then integrating that function

over a source made from the stress-energy tensor of the small body orbiting the BH; see [21] for specifics.

The radial Teukolsky equation possesses two asymptotic solutions that determine the behavior of ψ_4 at spatial infinity and near the event horizon. Far away, ψ_4 is related to the GWs carried from the system via $\psi_4 \to \frac{1}{2}(\ddot{h}_+ - i\ddot{h}_\times)$. Therefore, the solution to the radial Teukolsky equation that describes purely outgoing radiation at spatial infinity can be used to construct the flux of radiation and the waveform that distant observers measure. Near the event horizon, ψ_4 describes tidal interactions of the BH with the orbiting body [20]. The solution describing ingoing radiation at the horizon can be used to construct the radiation flux absorbed by the BH. With these fluxes, we can then calculate the rate at which the orbital radius changes, $\dot{r}$, by noting that for slow backreaction the system evolves through a sequence of geodesic orbits.

We compute ψ_4 on a grid of orbits from $r = 10\,000M$ to the Schwarzschild ISCO at $r = 6M$ (in Boyer-Lindquist coordinates), evenly spacing our orbits in $v \equiv \sqrt{M/r}$. (Stable circular orbits do not exist for $r < 6M$, so we cannot infer $\dot{r}$ from dE/dt here.) Errors in the Teukolsky-based waveforms are dominated by truncation of the (ℓ, m) sums in ψ_4 and by the discretization onto a grid in v. The sums and discretization are chosen such that the fractional error in the flux is smaller than 10^{-10} [21,22]. In the low velocity region $v < 0.1$, we find that the flux is accurate to at least 10^{-13}. Such an error translates to inaccuracies in the GW phase of less than 10^{-2} rad over a 2-year evolution.

Systems, regions and models.—To demonstrate the flexibility of the EOB model in matching the Teukolsky-based waveforms, we examine two fiducial EMRI systems, labeled systems I and II, that sample different regions of the LISA noise curve. In both cases, we consider a 2-year long quasicircular inspiral of nonspinning BHs. System I has $(m_1, m_2) = (10^5, 10)M_\odot$; system II has $(m_1, m_2) = (10^6, 10)M_\odot$. We do not consider lower or higher total mass binaries as they would either reach the ISCO outside the LISA optimal sensitivity band (LISA's noise rises sharply above $\sim 10^{-2}$ Hz) or lie significantly inside the white-dwarf confusion limit (much below ~ 0.002 Hz [25]). System II ($m_2/m_1 = 10^{-5}$) begins at an initial separation $r_{\text{in}} \simeq 10.6M$ and terminates at the ISCO, sweeping GW frequencies in the range $f_{\text{GW}} \in [1.8 \times 10^{-3}, 4.4 \times 10^{-3}]$ Hz. System I ($m_2/m_1 = 10^{-4}$) starts at $r_{\text{in}} \simeq 29.34M$ and terminates at $r_{\text{fin}} \simeq 16.1M$, sweeping frequencies in the range $f_{\text{GW}} \in [4 \times 10^{-3}, 10^{-2}]$ Hz. The mass ratios we consider, $(10^{-4}, 10^{-5})$ are 2 orders of magnitude smaller than those studied in the complementary analyses of [9,10]. As such, our in-band signal is dominated by a long inspiral; the contributions of the final plunge, merger, and ringdown, which dominate the signal of [9,10], are much less important here. These choices allow the study of the early and late EMRI dynamics, while guaranteeing the GW signal is in the sensitive part of the LISA band.

We define two EOB models differing in the resummation of the radiation-reaction force in Eq. (3). Using the balance law, we write $\hat{\mathcal{F}}_\Phi = -F/(\nu\Omega)$, where F is the GW energy flux. We use (i) the Padé approximant to the energy flux [13,23] $F^P = F_q^p(v_{pole})$, where v_{pole} is an adjustable parameter locating the EOB light ring, and $p + q$ is twice the approximant's PN order [i.e., $(v/c)^{(p+q)}$], and (ii) the ρ approximant to the energy flux [11] $F^\rho = 2/(16\pi)\sum_{\ell=2}^{\ell=8}\sum_{m=1}^{m=\ell}(m\Omega)^2|Rh_{\ell m}|^2$. Except when investigating the effect of the self-force, the orbital dynamics are computed setting $\nu = 0$ in F, as well as in $A(r)$ and $D(r)$.

Results.—Figure 1 shows the absolute value of the difference between the Newtonian-normalized ($F_{Newt} = 32\nu^2 v^{10}/5$) Teukolsky and EOB (uncalibrated and calibrated) fluxes as a function of the orbital velocity v. The Teukolsky flux includes energy radiated to infinity and absorbed by the BH's event horizon. The uncalibrated Padé flux (F_4^7) and ρ flux are computed through 5.5PN order, but in the Padé flux we also add horizon absorption corrections [26] and set v_{pole} to the Schwarzschild light-ring value. The uncalibrated Taylor flux (i.e., the PN Taylor-expanded flux [27]) gives a residual about 5 times worse than the uncalibrated Padé and ρ fluxes. The calibrated Padé flux (F_6^7) is computed through 6.5PN order, including the horizon absorption corrections, and calibrating v_{pole} and the 6PN and 6.5PN coefficients $\mathcal{F}_{12}$ and $\mathcal{F}_{13}$; see [27] for details. The calibrated ρ flux is computed through 6PN order, without horizon absorption corrections, and calibrating the 6PN coefficients $c_6^{\rho_{22}}$ in ρ_{22} and the 5PN coefficients $c_5^{\rho_{33}}$ in ρ_{33}; see [11] for details. The calibration is here performed via a least-squares fit to the numerical Teukolsky flux. For velocities $v \in [0.01, 0.1]$ the agreement is better than 10^{-8}, with agreement of 10^{-13} near $v = 0.01$ for all models.

Comparisons of Teukolsky-based and EOB waveforms are performed once they are aligned in time and phase. This guarantees that the fitting factor is maximized over time and phase of coalescence in a matched filtering calculation with white noise [13]. The alignment procedure depends sensitively on the alignment window chosen. We align the waveforms at low frequencies, in the interval $t \in [0, 64]\lambda_{GW}$, where λ_{GW} is the GW wavelength, $t \simeq (0, 0.006M)$ [$t \simeq (0, 0.013M)$] months for system I [system II], to a level of 10^{-10} [10^{-6}] rad in the phase for system I [system II]. We have checked that choosing any interval window of width $<2^9\lambda_{GW}$ changes the final dephasing by less than 10^{-3} rad and the relative amplitude difference by less than 10^{-6}.

In the left panel of Fig. 2 we plot the phase difference, or *dephasing*, between the dominant h_{22} mode of the Teukolsky-based and EOB waveforms as a function of time. We find that after 2 years the dephasing is ~ 40 (3000) rad for system I (system II) when using the EOB-model with Taylor flux (not shown in the figure) [27], in qualitative agreement with previous investigations [28]. The EOB-model with uncalibrated Padé flux at 5.5PN
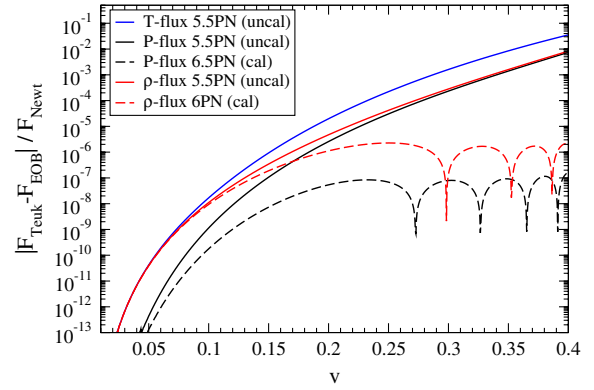

FIG. 1 (color online).   Absolute value of the difference in the Newtonian-normalized Teukolsky and EOB fluxes as a function of orbital velocity. Calibrating the Padé or ρ flux improves the agreement by orders of magnitude.

has a dephasing of ~ 5 (530) rad for system I (system II); this can be reduced to ~ 0.1 (0.01) rad using the calibrated Padé flux at 6.5PN. The EOB model with uncalibrated ρ flux at 5.5PN has a dephasing of ~ 10 (530) rad for system I (system II); this can be reduced to ~ 2 (0.8) rad with the calibrated ρ flux at 6PN.

In the right panel of Fig. 2, we compare the amplitude of the dominant mode $A_{22} = |h_{22}|$, computed in the EOB and Teukolsky frameworks. After 2 years of evolution, the calibrated Padé- and ρ-flux EOB models have a disagreement of $\sim 10^{-5}$ for system I and $\sim 2 \times 10^{-3}$ for system II. Such phase and amplitude agreement is fantastic when one takes into account the 2-year length of observation, during which system I (system II) evolves over 2×10^6 (9×10^5) rad. Interestingly, we find that if we switch on the relative ν terms in the 3PN EOB Hamiltonian Eq. (1) and in the flux, the dephasing for the EOB model with ρ flux at 6PN increases to ~ 27 (6) rad for system I (system II). (Adding the ν terms to the Hamiltonian amounts to accounting for the conservative self-force; adding those to the flux amounts to taking the dissipative self-force to higher order in mass ratio.) The main effect comes from the dissipative self-force, a result consistent with [29] for circular orbits.

We also compare the strongest higher harmonics using the EOB model with Padé flux at 6.5PN. In the case of the $(\ell, m) = (3, 3)$ and $(\ell, m) = (4, 4)$ modes we find dephasings of ~ 0.14 (0.07) and ~ 0.18 (0.09) rad, and normalized amplitude differences of $\sim 6 \times 10^{-5}$ (4×10^{-3}) and $\sim 3 \times 10^{-4}$ (9×10^{-3}), for system I (system II). These dephasings are comparable to those found for the $(\ell, m) = (2, 2)$ mode because in both frameworks the GW phase can be computed directly from the orbital phase. As a consequence, these comparisons are almost entirely governed by the trajectories of the test particle. Finally, we find that higher harmonics contribute significantly less to the signal-to-noise ratio relative to the (2, 2) mode. In particular, we computed the signal-to-noise ratio averaged over beam-pattern functions with a noise spectral density that includes
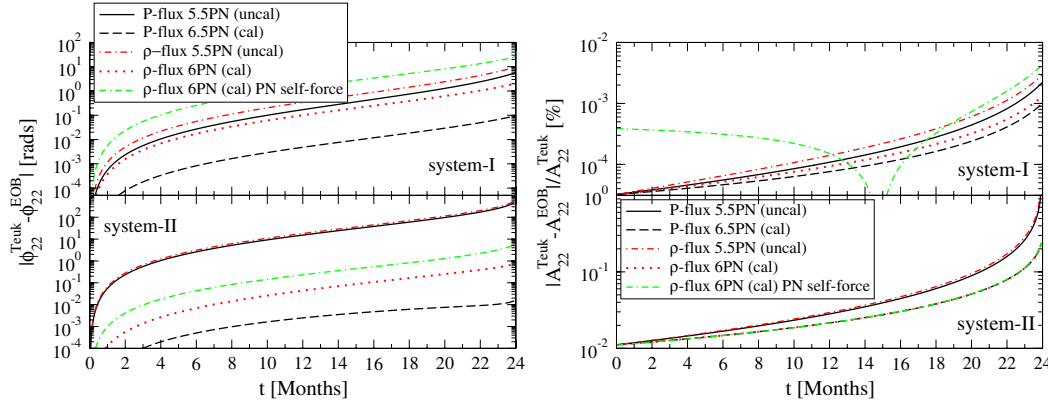
FIG. 2 (color online).   Absolute value of the dephasing (left) and fractional amplitude difference (right) of the dominant GW (2, 2) mode as a function of time in months. Again, with the introduction of calibrated higher-order terms, the differences are small even over a full 2 yr coherent integration.

white-dwarf confusion noise. Including up to $\ell = 5$ ($\ell = 7$) for system I (system II) guarantees a recovery of 97% of the total signal-to-noise ratio, with the $\ell = m$ modes dominating.

Data analysis implications and discussion.—These results demonstrate that the EOB framework can model EMRIs for LISA data analysis purposes, with the advantage of allowing for the consistent inclusion of both dissipative and conservative PN self-force terms. Such terms also allow the construction of waveforms from intermediate-mass ratio inspirals, where first-order BH perturbation theory is expected to fail. The comparisons made here, however, serve only as a proof of principle. One must now generalize to more generic spinning EMRIs, and to more complicated orbital geometries.

The EOB framework also allows us to provide, for the first time, a metric-based estimate of the number of templates needed for EMRI systems in LISA data analysis [23,30]. As a coherent 2-year integration in the search of EMRIs is computationally prohibitive, a hierarchical search that collects power from coherent searches of shorter segments was proposed in [1]. The maximum segment length set by computational limits in such a hierarchical search is estimated to be less than 2 months. For a 2-month evolution, we estimate that one requires less than 10^7 EOB templates to cover the template bank with a minimal match of 0.97 in the total mass range $(10^5 - 10^6) M_\odot$ and mass-ratio range $(10^{-4} - 10^{-5})$.

[1]   J. R. Gair, L. Barack, T. Creighton, C. Cutler, S. L. Larson, E. S. Phinney, and M. Vallisneri, Classical Quantum Gravity **21**, S1595 (2004).

[2]   S. A. Hughes, AIP Conf. Proc. **873**, 233 (2006).
[3]   A. Buonanno and T. Damour, Phys. Rev. D **59**, 084006 (1999).
[4]   A. Buonanno and T. Damour, Phys. Rev. D **62**, 064015 (2000).
[5]   T. Damour, P. Jaranowski, and G. Schafer, Phys. Rev. D **62**, 084011 (2000).
[6]   T. Damour, Phys. Rev. D **64**, 124013 (2001).
[7]   A. Buonanno, Y. Chen, and T. Damour, Phys. Rev. D **74**, 104005 (2006).
[8]   T. Damour, P. Jaranowski, and G. Schafer, Phys. Rev. D **77**, 064032 (2008).
[9]   A. Nagar, T. Damour, and A. Tartaglia, Classical Quantum Gravity **24**, S109 (2007).
[10]   T. Damour and A. Nagar, Phys. Rev. D **76**, 064028 (2007).
[11]   T. Damour, B. R. Iyer, and A. Nagar, Phys. Rev. D **79**, 064004 (2009).
[12]   T. Damour and A. Nagar, Phys. Rev. D **79**, 081503(R) (2009).
[13]   A. Buonanno *et al.*, Phys. Rev. D **79**, 124028 (2009).
[14]   P. Amaro-Seoane *et al.*, Classical Quantum Gravity **24**, R113 (2007).
[15]   M. C. Miller *et al.*, Astrophys. J. Lett. **631**, L117 (2005).
[16]   D. Syer, C. J. Clarke, and M. J. Rees, Mon. Not. R. Astron. Soc. **250**, 505 (1991).
[17]   Y. Levin, astro-ph/0307084.
[18]   Y. Levin, Mon. Not. R. Astron. Soc. **374**, 515 (2007).
[19]   J. Wang and D. Merritt, Astrophys. J. **600**, 149 (2004).
[20]   S. A. Teukolsky, Astrophys. J. **185**, 635 (1973).
[21]   S. A. Hughes, Phys. Rev. D **61**, 084004 (2000).
[22]   S. A. Hughes, Phys. Rev. D **64**, 064004 (2001).
[23]   T. Damour, B. R. Iyer, and B. S. Sathyaprakash, Phys. Rev. D **57**, 885 (1998).
[24]   R. Fujita and H. Tagoshi, Prog. Theor. Phys. **113**, 1165 (2005).
[25]   A. J. Farmer and E. S. Phinney, Mon. Not. R. Astron. Soc. **346**, 1197 (2003).
[26]   Y. Mino *et al.*, Prog. Theor. Phys. Suppl. **128**, 1 (1997).
[27]   M. Boyle *et al.*, Phys. Rev. D **78**, 104020 (2008).
[28]   I. Mandel and J. R. Gair, Classical Quantum Gravity **26**, 094036 (2009).
[29]   A. Pound and E. Poisson, Phys. Rev. D **77**, 044013 (2008).
[30]   B. J. Owen, Phys. Rev. D **53**, 6749 (1996).